

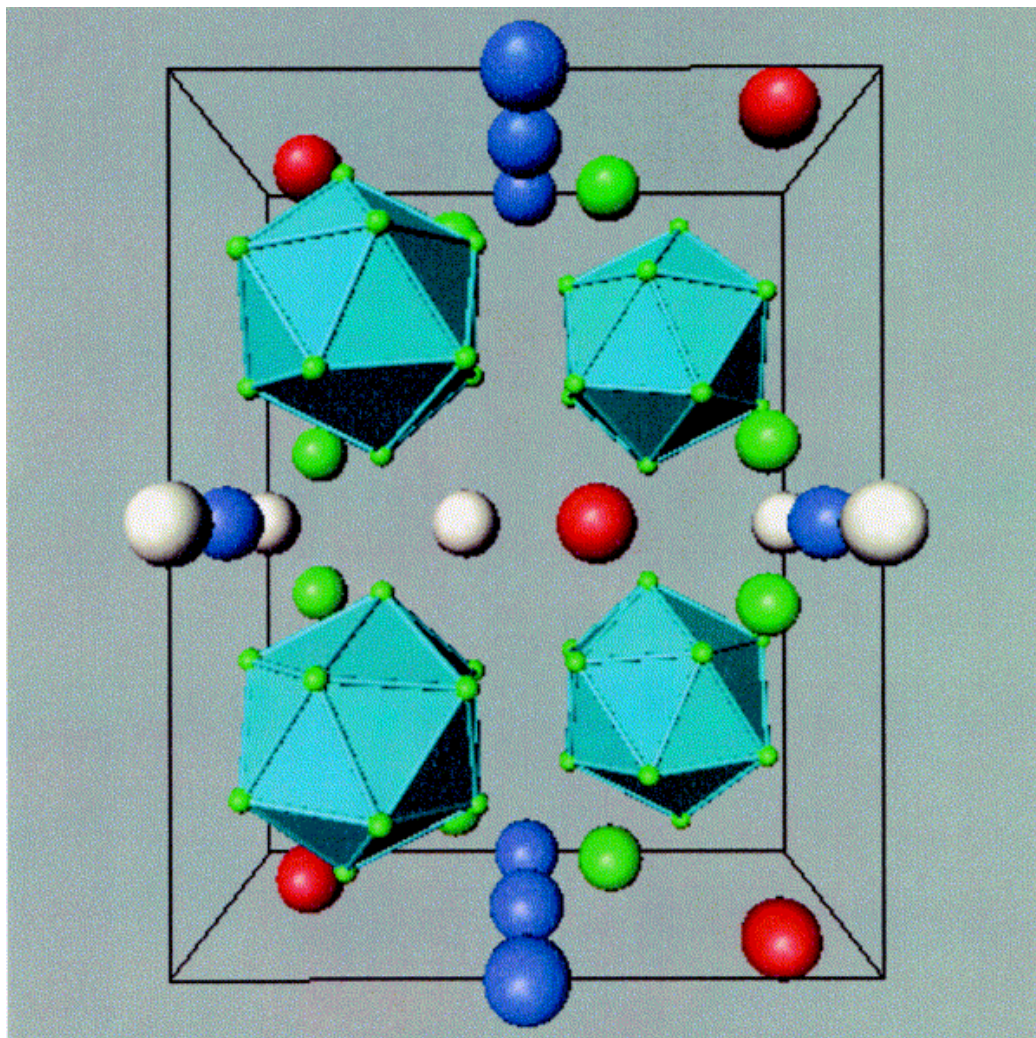
# **A Synthesis and Study of $\text{AlMgB}_{14}$**

**Richard Bodkin**

**A thesis presented to the University of the Witwatersrand in  
fulfilment of the requirements for the degree of Doctor of Philosophy**

**2005**

# A Synthesis and Study of $\text{AlMgB}_{14}$



by

**Richard Bodkin**

## **DECLARATION**

I, Richard Bodkin declare that this thesis is my own work. It is being submitted for the degree of Doctor of Philosophy at the University of the Witwatersrand, Johannesburg. It has not been submitted before for any degree or examination at any other university.

---

Richard Bodkin

This \_\_\_\_\_ day of \_\_\_\_\_, 2005

# Abstract

*This project is specifically concerned with the processing, densification and mechanical properties of hot-pressed  $\text{AlMgB}_{14}$ , a hard ceramic material. In order to gain a better understanding of the processing and densification of  $\text{AlMgB}_{14}$ , it was necessary to investigate the Al-Mg-B ternary phase diagram. The study conducted indicated that the continuous solid solution that exists at  $900^\circ\text{C}$  between  $\text{AlB}_2$  and  $\text{MgB}_2$  recedes towards  $\text{MgB}_2$  as the temperature is increased from  $900^\circ\text{C}$  to  $1400^\circ\text{C}$ . The position of the boundary was quantified using X-Ray diffraction and linear regression analysis to estimate the lattice constants. The results obtained using this method were confirmed by a Rietveld method. The final quantification of the solid solution boundary was done using the Rietveld results.*

*From the phase diagram studies it was shown that aluminium rich compositions of the elemental powders Al, Mg and B could be used to produce  $\text{AlMgB}_{14}$ . Specifically, composites that had a 3 wt.% excess of aluminium were found to produce the densest samples with the lowest porosities. As stated above samples were produced by hot-pressing. Hot-pressing was done on elemental powders of aluminium, magnesium and boron, at various loads between 20 and 75 MPa, temperatures between 900 and  $1900^\circ\text{C}$ , soak times of 1 hour and heating rates between 10 and  $100^\circ\text{C}/\text{min}$ .*

*It was found that for elemental powders, milled in a planetary ball mill with a WC milling media, of Al, Mg and B in the mole ratio of 1:1:14 did not produce  $\text{AlMgB}_{14}$  at temperatures of less than  $1200^\circ\text{C}$ . For compositions richer in aluminium  $\text{AlMgB}_{14}$  could be produced at temperatures of  $1000^\circ\text{C}$ . This suggests that the presence of the aluminium liquid phase aids with mass transport and thus the formation of  $\text{AlMgB}_{14}$  is facilitated. Pure  $\text{AlMgB}_{14}$  was not produced by this method and the predominant impurity was  $\text{MgAl}_2\text{O}_4$  ( $\approx 10$  wt.%).*

*It was found that this impurity phase is formed as a result of the oxide content in the starting elemental powders. The amount of  $\text{MgAl}_2\text{O}_4$  can be limited by removal of the  $\text{B}_2\text{O}_3$  from the starting powders. This is achieved by milling the starting powders in an*

alcohol, specifically, methanol.  $B_2O_3$  reacts with the methanol to produce boron esters which volatilise during evaporation of the milling solvent under a reduced pressure. It was also demonstrated that the milling of magnesium and aluminium in a planetary ball mill at 200-250 rpm did not further oxidise the aluminium and magnesium starting powders.

The optimum hot pressing parameters for producing dense  $AlMgB_{14}$  were found to be at a temperature of  $1600^\circ C$ , heating rate of  $100^\circ C/min$ , a pushing force of 75 MPa and a soak time of 1 hour. However, samples produced from elemental powders were found to have a preferred orientation perpendicular to the hot-pressing direction. This is not uncommon for hot-pressed materials in which there exists a liquid phase. It was also found that equally dense  $AlMgB_{14}$  could also be produced from micron sized pre-reacted elemental powders at the optimum hot-pressing conditions as those for the elemental powders. Pre-reacted powders were produced at  $1400^\circ C$ , 20 MPa,  $10^\circ C/min$  and 1 hour soak time. Compacts produced from the pre-reacted elemental powders were found to have no preferential alignment of homogeneous microstructure after hot-pressing at  $1600^\circ C$ , 75 MPa,  $100^\circ C/min$ . Samples prepared from the pre-reacted powders contain  $W_2B_5$  as a secondary phase due to wear associated with WC milling media.

Pre-reacted powders were admixed separately with the compounds  $TiB_2$ ,  $TiC$ ,  $TiN$ ,  $Si$  and  $WC$ . Additionally, a compact containing  $TiB_2$  and  $WC$  was also produced. Because of the reaction of the carbides and nitride with boron containing compounds, additional boron was added to those composites with the added nitrides and carbides in an attempt to minimise the reaction of those nitrides and carbides with the already formed boride phases in the pre-reacted powder. All the composites produced were found to contain only closed porosity ( $< 3\%$ ). The hardness and fracture toughness of these composites were measured from Vickers indents made at a 10 kg loading. The addition of  $TiB_2$  (29.5 GPa),  $TiC$  (32.1 GPa),  $TiB_2 + WC$  (29.1 GPa) and  $Si$  (31.2 GPa) to the baseline material,  $AlMgB_{14}$ , were found to increase the hardness of the baseline material (24 GPa). The addition of  $TiN$  did not increase the hardness of the baseline material.

*WC was found to react with boron and/or boride phases to form platelet-like  $W_2B_5$  grains. The formation of  $W_2B_5$  was prevalent in all the compacts because of the introduction of WC from the milling media and vessel. In the composites with Ti-based additions a solid solution  $(Ti,W)B_2$  formed. In composites produced with  $TiB_2$  a core-rim structure was observed by SEM. Composites based on the additions of TiC and TiN or those with additional boron were found to have no core-rim structure.*

*Composites produced from  $TiB_2 + WC +$  additional B increased the hardness of the baseline material from 24.0 GPa to 33.8 GPa and the fracture toughness from  $7.7 \text{ MPam}^{1/2}$  to  $9.8 \text{ MPam}^{1/2}$ .*

## **Dedication**

It is over! Thank God, Mathias and Candice.

## **Acknowledgements**

I would like to extend my gratitude and thanks to the following people:

### **School of Chemistry**

Neil, Marcus, Mike, Barry, Steve, Ewa, Jo, Charles, Martha, Agnes, Amanda, Colleen, Pat, Demi, Dave, Manuel and Paul.

### **School of Engineering**

Jack, Silvana, Graham, Theo, Aubrey, Bruce and Charmaine.

### **School of Physics**

John, Kurt, Shuan, Andrew and Charles.

### **Council for Scientific and Industrial Research**

Sara and Loukie.

### **Fraunhofer IKTS Dresden**

Mathias, for so much!

### **Element 6**

Hester, Brett, Peter, Lucas, Festus, Rod, Cheryl, Nick, Lex, James, Derrick, Lelanie and the company for a generous scholarship.

### **Colleagues and friends**

John and James.

### **Family**

Mom, Dad and Keith

### **Personal**

Candice, for your patience, love, and above all, your understanding.



## **TABLE OF CONTENTS**

<b>CHAPTER 1: INTRODUCTION</b>	<b>1</b>
1.1: Background and Motivation	1
1.2: Project Overview	3
<b>CHAPTER 2: LITERATURE REVIEW</b>	<b>4</b>
2.1: Hard Materials	4
2.1.1 Hardness	4
2.1.2: The traditional paradigm for a hard material	8
2.2: Boride-based hard materials	9
2.2.1: Chemical bonding and structure types of some borides	10
2.2.2: The structure of AlMgB <sub>14</sub>	11
2.2.3: The production of dense polycrystalline AlMgB <sub>14</sub> and associated impurity phases	13
2.2.4: Electrical, Thermal and Magnetic Properties of AlMgB <sub>14</sub>	14
2.2.5: The microhardness of polycrystalline AlMgB <sub>14</sub>	16
2.2.6: Elastic constants of polycrystalline AlMgB <sub>14</sub>	19
2.2.7: Thermal Expansion of polycrystalline AlMgB <sub>14</sub>	21
2.2.8: Applications of AlMgB <sub>14</sub>	23
2.2.9: Binary and Ternary Phase systems of interest	25
<b>CHAPTER 3: EXPERIMENTAL</b>	<b>26</b>
3.1: Chemicals	26
3.2: Equipment	27
3.2.1: Furnaces	27
3.2.1.1: The Tube Furnace	27
3.2.1.2: The Hot Isostatic Press	27
3.2.1.3: The Uniaxial Hot Press	28
3.2.1.4: Pyrolysis Furnace	31
3.2.2: The Planetary Mill	32
3.3: The Reaction Procedure	32
3.3.1: Preparing the Starting Powders	32

3.3.2: Compositions of the Powders	33
3.3.3: Sintering the Green Compacts	35
<b>3.4 Analytical Procedures</b>	<b>35</b>
3.4.1: Density Determination	35
3.4.2: Porosity by Image Analysis	36
3.4.3: Polishing of the Samples	36
3.4.4: X-Ray Diffraction	37
3.4.5: Particle Sizing	37
3.4.6: Scanning Electron Microscopy	38
3.4.7: Transmission Electron Microscopy	38
3.4.8: Inductively Coupled Plasma Analysis	38
3.4.9: Hardness and Fracture Toughness Testing	38
3.4.10: Thermal Analysis	39
 <b>CHAPTER 4: THE ALUMINIUM MAGNESIUM BORON TERNARY PHASE DIAGRAM</b>	 <b>40</b>
<b>4.1: Introduction</b>	<b>40</b>
4.1.1: The Aluminium-Boron Binary Phase Diagram	40
4.1.2: The Magnesium-Boron Binary Phase Diagram	42
4.1.3: The Al-Mg Binary System	44
4.1.4: The Aluminium-Magnesium-Boron Ternary Phase Diagram	46
4.1.5: The Solid Solution	48
<b>4.2: Experimental</b>	<b>49</b>
4.2.1: Qualitative XRD analysis	49
4.2.2: Quantitative XRD analysis	49
4.2.2: The XRD Scan Criteria	50
4.2.3: The Rietveld Method	53
<b>4.3: Results and Discussion</b>	<b>54</b>
4.3.1: The Compositions	54
4.3.2: Results of the Qualitative Analysis	56
4.3.3: The Thermodynamic Stability of the Phases	68
4.3.4: Quantifying the Phases using Rietveld Analysis	71
4.3.5: The Error in the 'a' and 'c' Parameter	75
4.3.6: Quantifying the Solid Solution Boundary	77
4.3.7: Composition 9 and the Volatilisation of Magnesium	81
4.3.8: Verifying the Phase Content for Composition 4	82

<b>4.4: Summary</b>	<b>84</b>
 <b>CHAPTER 5: LIMITING THE OXIDE PHASE</b>	 <b>87</b>
<b>5.1: Introduction</b>	<b>87</b>
5.1.1: Conventional Methods for Limiting Oxide Phase Formation	87
5.1.2: Measuring the Oxygen Content	89
5.1.3: Limiting the Formation of the Spinel Phase in AlMgB <sub>14</sub> materials	90
5.1.3.1: The MgAl <sub>2</sub> O <sub>4</sub> system	90
5.1.3.2: The AlMgB <sub>14</sub> compound	92
5.1.4: Boron Oxide as an oxidising agent	93
5.1.5: Boron as a reducing agent	93
5.1.6: Boron oxide and the formation of boron esters	94
 <b>5.2: Experimental</b>	 <b>95</b>
5.2.1: Solvent Properties	95
5.2.2: TEM analysis	98
 <b>5.3: Results and Discussion</b>	 <b>99</b>
5.3.1: Carbothermal Reduction	99
5.3.2: X-ray diffraction techniques	100
5.3.2.1: The baseline material	100
5.3.2.2: Washing the boron powder versus milling the boron powder in the solvent	102
5.3.2.3: The effect of milling Al, Mg and B in various solvents	104
5.3.2.4: Predicting the amount of spinel phase present in AlMgB <sub>14</sub> samples milled in alcohol	107
5.3.3: EDS analysis performed by TEM on boron powders milled in hexane and methanol	108
5.3.4: TEM analysis of the starting Mg and Al powders	109
 <b>5.4: Summary</b>	 <b>109</b>
 <b>CHAPTER 6: PROCESSING ALMGB<sub>14</sub></b>	 <b>111</b>
<b>6.1: Introduction</b>	<b>111</b>
6.1.1: The Ti-B-C Ternary Phase System	111
6.1.2: The Ti-B-N Ternary Phase System	113
6.1.3: The W-B-C Ternary Phase System	114
 <b>6.2: Experimental</b>	 <b>116</b>
 <b>6.3: Results and Discussion</b>	 <b>116</b>
6.3.1 Preliminary investigations of the formation of AlMgB <sub>14</sub>	116
6.3.2: A synthesis of AlMgB <sub>14</sub> from AlB <sub>12</sub> and MgB <sub>2</sub>	118

6.3.3: Additives in AlMgB <sub>14</sub>	121
6.3.3.1 AlMgB <sub>14</sub> + 30 wt.% TiB <sub>2</sub>	122
6.3.3.2: AlMgB <sub>14</sub> + 20 wt.% TiN	125
6.3.3.3: AlMgB <sub>14</sub> + 20 wt.% TiC	127
6.3.3.4: AlMgB <sub>14</sub> + 20 wt.% TiCN	130
6.3.3.5: AlMgB <sub>14</sub> + 20 wt.% WC	133
6.3.4: The Production of Dense AlMgB <sub>14</sub>	135
6.3.4.1: The Effect of Particle Size	135
6.3.4.2: The Effect of Composition	138
6.3.4.3: The Effect of Temperature	141
6.3.4.4: The Effect of Pressure	143
6.3.4.5: Pre-Reacted Powder versus Elemental Powders	144
6.3.5: Microstructure and Mechanical Properties of compacts based on AlMgB <sub>14</sub>	148
6.3.5.1: The hardness of composites produced from pre-reacted AlMgB <sub>14</sub>	149
6.3.5.2: The PR <sub>3CS</sub> system	150
6.3.5.3: PR <sub>3CS</sub> + 30 wt.% TiB <sub>2</sub>	152
6.3.5.4: PR <sub>3CS</sub> + 5 wt.% Si	155
6.3.5.5: PR <sub>3CS</sub> + 25.8 wt.% TiC	157
6.3.5.6: PR <sub>3CS</sub> + 26.7 wt.% TiN	161
6.3.5.7 PR <sub>3CS</sub> + WC	164
6.3.5.8: PR <sub>3CS</sub> + 30 wt.% TiB <sub>2</sub> + 30 wt.% WC	170
6.3.5.9: The hardness and fracture toughness of the prepared composites	175
<b>6.4: Summary</b>	<b>179</b>
 <b>CHAPTER 7: CONCLUSIONS AND FUTURE WORK</b>	 <b>182</b>
 <b>REFERENCES</b>	 <b>185</b>
 <b>APPENDIX A</b>	 <b>191</b>

## **LIST OF FIGURES**

FIGURE 2.1.1: THE SCATTERING OF THE VICKERS HARDNESS MEASUREMENTS FOR VARIOUS HARD MATERIALS WHEN COMPARED WITH THEIR CORRESPONDING BULK (GREY AREA) AND SHEAR (BLUE AREA) MODULI <sup>10</sup>	5
FIGURE 2.1.2: A COMMON LOAD-HARDNESS RELATIONSHIP <sup>12</sup>	6
FIGURE 2.1.3: $H_{V1}$ FOR A FINE-GRAINED SINTERED ALUMINA CERAMIC PREPARED BY A SOL-GEL APPROACH STARTING WITH BOEHMITE <sup>13</sup>	7
FIGURE 2.2.1: A TYPICAL FIVE-FOLD SYMMETRIC ICOSAHEDRON	10
FIGURE 2.2.2: THE STRUCTURE OF $B_4C$ IN THE CHAIN OR POLAR STRUCTURES <sup>21</sup>	11
FIGURE 2.2.3: CRYSTAL STRUCTURE OF $AlMgB_{14}$ PROJECTION ON THE $AB$ PLANE	12
FIGURE 2.2.5 B: A PLOT OF THE ELECTRICAL RESISTIVITY IN $AlMgB_{14}$ AS A FUNCTION OF THE TOTAL VOLUME PERCENT OF $Al_2MgO_4$ , $Fe_3O_4$ AND FEB IMPURITY PHASES <sup>27</sup>	15
FIGURE 2.2.5: A PLOT OF THE MEAN MICROHARDNESS AS A FUNCTION OF THE TOTAL VOLUME PERCENT OF $Al_2MgO_4$ , $Fe_3O_4$ AND FEB IMPURITY PHASES IN $AlMgB_{14}$ . ERROR BARS INDICATE ONE STANDARD DEVIATION. NO LOAD HAS BEEN SPECIFIED FOR THE MICROHARDNESS MEASUREMENT <sup>27</sup>	17
FIGURE 2.2.6: PLOT OF MICROHARDNESS ( $H_{V1}$ ) VS. SHEAR MODULUS FOR VARIOUS MATERIALS <sup>10</sup> . THE FILLED CIRCLE SHOWS THE POSITION OF $AlMgB_{14}$ (NO LOAD HAS BEEN SPECIFIED FOR THIS MEASUREMENT) <sup>28</sup>	19
FIGURE 2.2.7: PART OF THE STRUCTURE OF $AlMgB_{14}$ SHOWING THE LOCATIONS OF AL AND MG RELATIVE TO THE B ICOSAHEDRA <sup>4</sup>	20
FIGURE 2.2.8: CRACK DEFLECTION AROUND $TiB_2$ PARTICLES IN A $B_4C$ MATRIX <sup>34</sup>	22
FIGURE 2.2.9: FLANK AND NOSE WEAR VS. CUTTING TIME FOR UNCOATED AND COATED TOOLS IN DRY MACHINING <sup>36</sup>	24
FIGURE 3.2.1: THE UNIAXIAL HOT PRESS	28
FIGURE 3.2.2: HOT-ZONE COMPONENTS USED IN THE UNIAXIAL HOT PRESS	29
FIGURE 3.2.2: CALIBRATION OF THE HOT PRESS' OPTICAL PYROMETER WITH AN HOT WIRE PYROMETER	30
FIGURE 3.2.3: A THERMO-GRAVIMETRIC PROFILE FOR $AlMgB_{14}$ + 3 WT.% PARAFFIN AND 5 WT. % STEARIC ACID IN ARGON, HEATING RATE 5°C/MIN	31
FIGURE 4.1.1: THE ALUMINIUM-BORON BINARY PHASE DIAGRAM REPRODUCED FROM THE REVIEW OF THE AL-B SYSTEM GIVEN BY O. N. CARLSON <sup>49</sup>	41
FIGURE 4.1.2: THE MAGNESIUM-BORON BINARY PHASE DIAGRAM <sup>50</sup>	43
FIGURE 4.1.3: THE AL-MG BINARY PHASE DIAGRAM <sup>53</sup>	45
FIGURE 4.1.4: AN ISOTHERMAL SECTION OF THE AL-MG-B TERNARY PHASE DIAGRAM AT 900°C <sup>57</sup>	47
FIGURE 4.2.1: XRD PATTERN FOR COMPOSITION 1 AT 900°C WITH 5 WT% SILICON AS AN INTERNAL STANDARD	50

FIGURE 4.2.2: LINEAR EQUATION FOR THE SHIFTING OF THE DIFFRACTOGRAM FOR COMPOSITION 1	51
FIGURE 4.3.1: COMPOSITIONS FOR THE STUDY OF THE AL-MG-B TERNARY PHASE DIAGRAM	54
FIGURE 4.3.2 A: DIFFRACTOGRAM FOR COMPOSITION 1 AT 900°C	56
FIGURE 4.3.2 B: DIFFRACTOGRAM FOR COMPOSITION 1 AT 1000°C	56
FIGURE 4.3.2 C: DIFFRACTOGRAM FOR COMPOSITION 1 AT 1200°C	57
FIGURE 4.3.2 D: DIFFRACTOGRAM FOR COMPOSITION 1 AT 1400°C	57
FIGURE 4.3.3: COMPARISON OF THE DIFFRACTOGRAMS FOR COMPOSITION 1	58
FIGURE 4.3.4: COMPARISON OF THE DIFFRACTOGRAMS FOR COMPOSITION 2	59
FIGURE 4.3.5: COMPARISON OF THE DIFFRACTOGRAMS FOR COMPOSITION 3	60
FIGURE 4.3.6: COMPARISON OF THE DIFFRACTOGRAMS FOR COMPOSITION 8	65
FIGURE 4.3.7: COMPARISON OF THE DIFFRACTOGRAMS FOR COMPOSITION 10	66
FIGURE 4.3.8 A: COMPOSITION 4 HEATED FOR 1 HOUR AND 5 HOURS AT 900°C	68
FIGURE 4.3.8 B: COMPOSITION 5 HEATED FOR 1 HOUR AND 5 HOURS AT 900°C	69
FIGURE 4.3.8 C: COMPOSITION 6 HEATED FOR 1 HOUR AND 5 HOURS AT 900°C	69
FIGURE 4.3.8 D: COMPOSITION 9 HEATED FOR 1 HOUR AND 5 HOURS AT 900°C	70
FIGURE 4.3.8 E: COMPOSITION 8 PREPARED AT 1200°C FOR 1 HOUR AND REHEATED FOR 5 HOURS AT 900°C	71
FIGURE 4.3.9: SCHEMATIC OF THE EQUILIBRIUM PHASES PREDICTED FOR COMPOSITIONS 1, 4 AND 8 AT THE 1000°C AND 1200°C TEMPERATURES	72
FIGURE 4.3.10: SHIFTED COMPOSITIONS 1, 4 AND 8 IN THE TERNARY PHASE DIAGRAM	75
FIGURE 4.3.11: TESTING VEGARD'S LAW FOR THE CHANGE IN THE 'A' AND 'C' PARAMETER FOR PURE MGB <sub>2</sub> AND PURE ALB <sub>2</sub>	76
FIGURE 4.3.12 A: RIETVELD AND METHOD 1 DETERMINATION OF THE %ALB <sub>2</sub> IN THE SOLID SOLUTION FROM COMPOSITION 4 AT 900, 1000, 1200 AND 1400°C	79
FIGURE 4.3.12 A: RIETVELD AND METHOD 1 DETERMINATION OF THE %ALB <sub>2</sub> IN THE SOLID SOLUTION FROM COMPOSITION 8 AT 900, 1000, 1200 AND 1400°C	79
FIGURE 4.3.13: COMPOSITION OF THE SOLID SOLUTION BASED ON THE RIETVELD REFINEMENT DATA FOR COMPOSITION 4	80
FIGURE 4.3.14: SHIFTED COMPOSITION 9 DETERMINED FROM THE COMPOSITION OF THE SOLID SOLUTION	81
FIGURE 4.3.15: TIE LINES DRAWN IN THE ISOTHERMAL SECTION OF THE AL-MG-B TERNARY PHASE DIAGRAM FOR COMPOSITION 4 AT 1000°C	83
FIGURE 4.4.1: A CROSS SECTION AT 66 AT.% B IN THE AL-MG-B TERNARY PHASE DIAGRAM	84
FIGURE 4.4.2 A: ISOTHERMAL SECTION OF THE AL-MG-B TERNARY PHASE DIAGRAM AT 1000°C	85
FIGURE 4.4.2 B: ISOTHERMAL SECTION OF THE AL-MG-B TERNARY PHASE DIAGRAM AT 1200°C	85

FIGURE 4.4.2 C: ISOTHERMAL SECTION OF THE AL-MG-B TERNARY PHASE DIAGRAM AT 1400°C	86
FIGURE 5.1.1: THE STRUCTURE OF $\text{MgAl}_2\text{O}_4$ THE GREY COLOURED ATOMS ARE MAGNESIUM CATIONS, THE GREEN COLOURED ATOMS ARE THE ALUMINIUM CATIONS AND THE RED ATOMS ARE THE OXYGEN ANIONS	91
FIGURE 5.3.1: OXYGEN CONTENT IN MG POWDER DETERMINED BY CARBOTHERMAL REDUCTION	99
FIGURE 5.3.2: X-RAY DIFFRACTOGRAM FOR RIETVELD ANALYSIS OF PHASE CONTENT	101
FIGURE 5.3.3: RIETVELD ANALYSIS DIFFRACTOGRAM	101
FIGURE 5.3.4: X-RAY DIFFRACTOGRAMS FOR SAMPLES PREPARED BY DIFFERENT METHODS HOT-PRESSED AT 1400°C, 20 MPA, 1 HOUR	103
FIGURE 5.3.5: DIFFRACTOGRAM FOR THE MILLED SAMPLE HOT-PRESSED AT 1400°C, 20 MPA, 1 HOUR	104
FIGURE 5.3.6 A: RATIO OF BORIDE/OXIDE VS. SOLVENT	105
FIGURE 5.3.6 B: RATIO OF BORIDE/OXIDE VS. ALCOHOL SOLVENT POLARITY	106
FIGURE 6.1.1: AN ISOTHERMAL SECTION AT 1400°C FOR THE TI-B-C TERNARY PHASE DIAGRAM <sup>94</sup>	112
FIGURE 6.1.2: AN ISOTHERMAL SECTION AT 1500°C FOR THE TI-B-N TERNARY PHASE DIAGRAM <sup>101</sup>	113
FIGURE 6.1.3: AN ISOTHERMAL SECTION AT 1500°C FOR THE W-B-C TERNARY PHASE DIAGRAM <sup>103</sup>	115
FIGURE 6.3.1: A COMPARISON OF THE DIFFRACTOGRAMS FOR $\text{AlMgB}_{14}$ PRODUCED IN THE TUBE, HIP AND UNIAXIAL HOT PRESS FURNACES AT 1400°C	116
FIGURE 6.3.2: MICROSTRUCTURE OF $\text{AlMgB}_{14}$ MADE AT 1400°C AND 20 MPA IN A HOT PRESS	118
FIGURE 6.3.3: DIFFRACTOGRAM FOR $\text{AlB}_{12} + \text{MgB}_2$ PREPARED AT 1400°C FOR 1 HOUR	120
FIGURE 6.3.4A: IDENTIFIED PHASES IN $\text{AlMgB}_{14} + 30 \text{ WT.}\% \text{ TiB}_2$	123
FIGURE 6.3.4 B: $\text{AlMgB}_{14} + 30 \text{ WT.}\% \text{ TiB}_2$ EXPANDED $2\theta$ REGION. THE EXPERIMENTAL DATA ARE COMPARED TO A SIMULATED SCAN FROM THE JCPDS DATA	124
FIGURE 6.3.4 C: THE MICROSTRUCTURE OF $\text{AlMgB}_{14} + 30 \text{ WT.}\% \text{ TiB}_2$	124
FIGURE 6.3.5 A: IDENTIFIED PHASES IN $\text{AlMgB}_{14} + 20 \text{ WT.}\% \text{ TiN}$	125
FIGURE 6.3.5 B: $\text{AlMgB}_{14} + 20 \text{ WT.}\% \text{ TiN}$ EXPANDED $2\theta$ REGION. THE EXPERIMENTAL DATA ARE COMPARED TO A SIMULATED SCAN FROM THE JCPDS DATA	126
FIGURE 6.3.5 C: THE MICROSTRUCTURE OF $\text{AlMgB}_{14} + 20 \text{ WT.}\% \text{ TiN}$	127
FIGURE 6.3.6 A: IDENTIFIED PHASES IN $\text{AlMgB}_{14} + 20 \text{ WT.}\% \text{ TiC}$	128
FIGURE 6.3.6 B: $\text{AlMgB}_{14} + 20 \text{ WT.}\% \text{ TiC}$ EXPANDED $2\theta$ REGION. THE EXPERIMENTAL DATA ARE COMPARED TO A SIMULATED SCAN FROM THE JCPDS DATA	129
FIGURE 6.3.6 C: THE MICROSTRUCTURE OF 20 WT.% TiC + $\text{AlMgB}_{14}$	129

FIGURE 6.3.7 A: IDENTIFIED PHASES IN ALMGB <sub>14</sub> + 20 WT.% TiCN	130
FIGURE 6.3.7 B: IDENTIFIED PHASES IN ALMGB <sub>14</sub> + 20 WT.% TiCN. THE EXPERIMENTAL DATA ARE COMPARED TO A SIMULATED SCAN FROM THE JCPDS DATA	131
FIGURE 6.3.7 C: THE MICROSTRUCTURE OF ALMGB <sub>14</sub> + 20 WT.% TiCN	131
FIGURE 6.3.8: COMPARISON OF THE DIFFRACTOGRAMS OBTAINED FOR ALL THE COMPOSITES PREPARED FROM THE Ti BASED ADDITIONS TO ALMGB <sub>14</sub>	132
FIGURE 6.3.9 A: IDENTIFIED PHASES IN ALMGB <sub>14</sub> + 20 WT.% WC	133
FIGURE 6.3.9 B: THE MICROSTRUCTURE OF ALMGB <sub>14</sub> + 20 WT.% WC	134
FIGURE 6.3.10: MASS PERCENT OF TUNGSTEN VERSUS MILLING TIME FOR PRE-REACTED POWDERS	137
FIGURE 6.3.11: COMPARISON OF ELEMENTAL AND PRE-REACTED ALMGB <sub>14</sub> (6 HOURS MILLING) WITH W <sub>2</sub> B <sub>5</sub>	138
FIGURE 6.3.12: A COMPARISON OF ALMGB <sub>14</sub> AND ALMGB <sub>14</sub> + COMPENSATION FOR THE SPINEL PHASE	140
FIGURE 6.3.13 A: COMPARISON OF THE XRD PATTERNS FOR ALMGB <sub>14</sub> PREPARED AT 900, 1200, 1400, 1600 AND 1700°C	141
FIGURE 6.3.13 B: X-RAY DIFFRACTOGRAM FOR ALMGB <sub>14</sub> PREPARED AT 1600°C	142
FIGURE 6.3.14 A: A MICROSCOPE IMAGE TAKEN FOR A COMPACT PRODUCED FROM THE ELEMENTAL STARTING POWDER WITH COMPOSITION A + CS + 3 WT.% AL AT 1600°C AND 75 MPA IN AN UNIAXIAL HOT-PRESS	147
FIGURE 6.3.14 B: A MICROSCOPE IMAGE TAKEN AT FOR A COMPACT PRODUCED FROM THE PRE-REACTED STARTING POWDER WITH COMPOSITION A + CS + 3 WT.% AL AT 1600°C AND 75 MPA IN AN UNIAXIAL HOT-PRESS	147
FIGURE 6.3.15A: DIFFRACTOGRAM FOR PR <sub>3CS</sub> REACTED AT 1600°C, HEATING RATE 100°C/MIN, SOAK TIME 1 HOUR, PRESSING FORCE 75 MPA	150
FIGURE 6.3.15 B: A COMPARISON OF UNREACTED PR <sub>3CS</sub> WITH REACTED PR <sub>3CS</sub>	151
FIGURE 6.3.15 C: AN SEM IMAGE FOR PR <sub>3CS</sub>	152
FIGURE 6.3.16 A: DIFFRACTOGRAM FOR PR <sub>3CS</sub> + 30 WT.% TiB <sub>2</sub> REACTED AT 1600°C, HEATING RATE 100°C/MIN, SOAK TIME 1 HOUR, PRESSING FORCE 75 MPA	153
FIGURE 6.3.16 B: AN SEM IMAGE FOR PR <sub>3CS</sub> + 30 WT.% TiB <sub>2</sub>	154
FIGURE 6.3.17 A: DIFFRACTOGRAM FOR PR <sub>3CS</sub> + 5 WT.% Si REACTED AT 1600°C, HEATING RATE 100°C/MIN, SOAK TIME 1 HOUR, PRESSING FORCE 75 MPA	155
FIGURE 6.3.17 B: A COMPARISON OF UNREACTED PR <sub>3CS</sub> + 5 WT.% Si WITH REACTED PR <sub>3CS</sub> + 5 WT.% Si	156
FIGURE 6.3.17 C: AN SEM IMAGE FOR PR <sub>3CS</sub> + 5 WT.% Si	156
FIGURE 6.3.18 A: DIFFRACTOGRAM FOR PR <sub>3CS</sub> + 25.8 WT.% TiC REACTED AT 1600°C, HEATING RATE 100°C/MIN, SOAK TIME 1 HOUR, PRESSING FORCE 75 MPA	157
FIGURE 6.3.18 B: A COMPARISON OF UNREACTED PR <sub>3CS</sub> + 25.8 WT.% TiC WITH REACTED PR <sub>3CS</sub> + 25.8 WT.% TiC	158



FIGURE 6.3.18 C: A COMPARISON OF REACTED $\text{PR}_{3\text{CS}}$ + 25.8 WT.% TIC WITH REACTED $\text{PR}_{3\text{CS}}$ + 25.8 WT.% TIC + 21.8 WT.% B	158
FIGURE 6.3.18 D: A PHASE ANALYSIS OF REACTED $\text{PR}_{3\text{CS}}$ + 25.8 WT.% TIC WITH REACTED $\text{PR}_{3\text{CS}}$ + 25.8 WT.% TIC + 21.8 WT.% B	159
FIGURE 6.3.18 E: AN SEM IMAGE FOR $\text{PR}_{3\text{CS}}$ + 25.8 WT.% TIC	160
FIGURE 6.3.18 F: AN SEM IMAGE FOR $\text{PR}_{3\text{CS}}$ + 25.8 WT.% TIC + 21.8 WT.% B	160
FIGURE 6.3.19 A: DIFFRACTOGRAM FOR $\text{PR}_{3\text{CS}}$ + 26.7 WT.% TIN REACTED AT 1600°C, HEATING RATE 100°C/MIN, SOAK TIME 1 HOUR, PRESSING FORCE 75 MPA	161
FIGURE 6.3.19 B: A COMPARISON OF UNREACTED $\text{PR}_{3\text{CS}}$ + 26.7 WT.% TIN WITH REACTED $\text{PR}_{3\text{CS}}$ + 26.7WT% TIN	162
FIGURE 6.3.19 C: A COMPARISON OF REACTED $\text{PR}_{3\text{CS}}$ + 26.7 WT.% TIN WITH REACTED $\text{PR}_{3\text{CS}}$ + 26.7WT% TIN + 15.7 WT.% B	162
FIGURE 6.3.19 D: AN SEM IMAGE FOR $\text{PR}_{3\text{CS}}$ + 26.7 WT.% TIN	163
FIGURE 6.3.19 D: AN SEM IMAGE FOR $\text{PR}_{3\text{CS}}$ + 26.7 WT.% TIN +15.7 WT.% B	163
FIGURE 6.3.20 A: DIFFRACTOGRAM FOR $\text{PR}_{3\text{CS}}$ + 15 WT.% WC REACTED AT 1600°C, HEATING RATE 10°C/MIN, SOAK TIME 1 HOUR, PRESSING FORCE 75 MPA	164
FIGURE 6.3.20 B: A COMPARISON OF $\text{PR}_{3\text{CS}}$ + 15 WT.% WC AND $\text{PR}_{3\text{CS}}$ + 30 WT.% WC REACTED AT 1600°C, HEATING RATE 10°C/MIN, SOAK TIME 1 HOUR, PRESSING FORCE 75 MPA	165
FIGURE 6.3.20 C: A COMPARISON OF $\text{PR}_{3\text{CS}}$ + 30 WT.% WC REACTED AT 1600°C, HEATING RATE 100°C/MIN AND 10°C/MIN, SOAK TIME 1 HOUR, PRESSING FORCE 75 MPA	165
FIGURE 6.3.20 D: DIFFRACTOGRAM FOR $\text{PR}_{3\text{CS}}$ + 30 WT.% WC REACTED AT 1600°C, HEATING RATE 100°C/MIN, SOAK TIME 1 HOUR, PRESSING FORCE 75 MPA	166
FIGURE 6.3.20 E: A COMPARISON OF REACTED $\text{PR}_{3\text{CS}}$ + 30.0 WT.% WC WITH REACTED $\text{PR}_{3\text{CS}}$ + 30.0WT% WC + 17.7 WT.% B	167
FIGURE 6.3.20 F: AN SEM IMAGE FOR $\text{PR}_{3\text{CS}}$ + 15.0 WT.% WC, HEATING RATE 10°C/MIN	168
FIGURE 6.3.20 G: AN SEM IMAGE FOR $\text{PR}_{3\text{CS}}$ + 15.0 WT.% WC, HEATING RATE 100°C/MIN	168
FIGURE 6.3.20 H: AN SEM IMAGE FOR $\text{PR}_{3\text{CS}}$ + 30.0 WT.% WC, HEATING RATE 10°C/MIN	169
FIGURE 6.3.20 I: AN SEM IMAGE FOR $\text{PR}_{3\text{CS}}$ + 30.0 WT.% WC, HEATING RATE 100°C/MIN	169
FIGURE 6.3.20 J: AN SEM IMAGE FOR $\text{PR}_{3\text{CS}}$ + 30.0 WT.% WC + 17.7 WT.% B, HEATING RATE 100°C/MIN	170
FIGURE 6.3.21 A: DIFFRACTOGRAM FOR $\text{PR}_{3\text{CS}}$ + 30 WT.% $\text{TIB}_2$ + 30 WT.% WC REACTED AT 1600°C, HEATING RATE 100°C/MIN, SOAK TIME 1 HOUR, PRESSING FORCE 75 MPA	171
FIGURE 6.3.21 B: THE PHASES PRESENT IN REACTED $\text{PR}_{3\text{CS}}$ + 30 WT.% $\text{TIB}_2$ + 30 WT.% WC AND REACTED $\text{PR}_{3\text{CS}}$ + 30 WT.% $\text{TIB}_2$ + 30WT% WC + 14.2 WT.% B	171
FIGURE 6.3.21 C: AN SEM IMAGE OF $\text{PR}_{3\text{CS}}$ + 30 WT.% $\text{TIB}_2$ + 30 WT.% WC	172
FIGURE 6.3.21 D: AN SEM IMAGE OF $\text{PR}_{3\text{CS}}$ + 30 WT.% $\text{TIB}_2$ + 30 WT.% WC + 14.2 WT.% B	172
FIGURE 6.3.22: A TYPICAL VICKERS INDENT AT A 10 KG LOADING	175

## **LIST OF TABLES**

TABLE 2.1: DENSITY, HARDNESS, BULK AND SHEAR MODULI OF SELECTED HARD MATERIALS <sup>2</sup>	18
TABLE 2.2: COEFFICIENT OF THERMAL EXPANSION OF SOME IMPORTANT HARD MATERIALS	21
TABLE 3.1.1: CHEMICALS USED FOR PROCESSING	26
TABLE 4.1.1: STRUCTURAL DATA FOR PHASES IN THE AL-B SYSTEM	42
TABLE 4.1.2: STRUCTURAL DATA FOR THE PHASES IN THE MG-B SYSTEM	43
TABLE 4.1.3: STRUCTURAL DATA FOR THE PHASES IN THE AL-MG BINARY PHASE DIAGRAM	45
TABLE 4.1.4: STRUCTURAL DATA OF ALMGB <sub>14</sub>	47
TABLE 4.2.1: 2 THETA PEAKS FOR ALB <sub>2</sub> , MGB <sub>2</sub>	50
TABLE 4.2.2: VALUES OF 1/D <sup>2</sup> CALCULATED AND 1/D <sup>2</sup> EXPERIMENTAL	52
TABLE 4.3.1: ATOMIC PERCENT FOR THE COMPOSITIONS	55
TABLE 4.3.2: SUMMARY OF THE MAJOR PHASES FOR COMPOSITION 9	62
TABLE 4.3.3: THE SHIFT IN D-SPACE FOR COMPOSITION 9 AT THE DIFFERENT TEMPERATURES	62
TABLE 4.3.4: SUMMARY OF THE MAJOR PHASES FOR COMPOSITIONS 1-3	63
TABLE 4.3.5: SUMMARY OF THE MAJOR PHASES FOR COMPOSITIONS 4-6	63
TABLE 4.3.6: SUMMARY OF THE MAJOR PHASES IDENTIFIED FOR COMPOSITION 8 AND 10	66
TABLE 4.3.7: RIETVELD ANALYSIS DATA FOR THE DETERMINATION OF THE PHASE CONTENT IN COMPOSITION 1, 4 AND 8	73
TABLE 4.3.8: ATOMIC PERCENT FOR UNSHIFTED AND SPINEL SHIFTED COMPOSITIONS	74
TABLE 4.3.9: THE CALCULATED CELL PARAMETERS FROM THE RIETVELD REFINEMENT	77
TABLE 4.3.10: CALCULATED LATTICE PARAMETERS USING METHOD 1	78
TABLE 4.3.11: COMPOSITION OF THE SOLID SOLUTION DETERMINED BY METHOD 1 AND THE RIETVELD METHOD	78
TABLE 4.3.12: CONCENTRATION OF ALB <sub>2</sub> IN (ALB <sub>2</sub> ) <sub>ss</sub> FOR COMPOSITION 9 DETERMINED BY METHOD 1	81
TABLE 4.3.13: COMPOSITION OF PHASES THAT CONTAIN ALL OF AL, MG AND B ONLY FOR COMPOSITION 4 FROM RIETVELD ANALYSIS AND CALCULATED FROM THE STARTING COMPOSITIONS	82
TABLE 5.2.1: PROPERTIES OF SOME ORGANIC COMPOUNDS	95
TABLE 5.2.2: THE CORRESPONDING BORON ESTERS	96
TABLE 5.3.1: TABLE OF PHASE CONTENT OF BASELINE ALMGB <sub>14</sub> DETERMINED BY RIETVELD ANALYSIS	102

TABLE 5.3.2: VALUES USED IN FIGURES 5.3.6A-B	105
TABLE 5.3.3: THE PERCENTAGE BY MASS OF THE SPINEL PHASE	107
TABLE 5.3.4: OXYGEN CONTENT IN THE POLYMER COATING	108
TABLE 5.3.5: MASS PERCENT OF OXYGEN IN BORON	108
TABLE 6.1.1: STRUCTURAL DATA FOR THE PHASES IN THE TI-B-C TERNARY PHASE DIAGRAM	112
TABLE 6.1.2: STRUCTURAL DATA FOR THE PHASES IN THE TI-B-N TERNARY PHASE DIAGRAM	114
TABLE 6.1.3: STRUCTURAL DATA FOR THE PHASES IN THE W-B-C TERNARY PHASE DIAGRAM	115
TABLE 6.3.1: PHASES, DENSITY AND POROSITY FOR ALMGB <sub>14</sub> PREPARED THE THREE DIFFERENT FURNACES	117
TABLE 6.3.2: DENSITY AND POROSITY OF ALB <sub>12</sub> , MGB <sub>2</sub> AND THE COMPOSITE ALB <sub>12</sub> + MGB <sub>2</sub>	121
TABLE 6.3.3: DENSITY, POROSITY AND MAJOR PHASES FOR ALMGB <sub>14</sub> COMPOSITES	122
TABLE 6.3.4 A: PROPERTIES OF ELEMENTAL POWDERS HOT-PRESSED AT 1400°C, 20 MPA, 1 HOUR	136
TABLE 6.3.4 B: PROPERTIES OF PRE-REACTED POWDERS HOT-PRESSED AT 1400°C, 20 MPA, 1 HOUR	136
TABLE 6.3.5: THE DENSITIES, POROSITIES AND THEORETICAL DENSITIES FOR ELEMENTAL ALMGB <sub>14</sub> PREPARED WITH EXCESS MAGNESIUM AND/OR ALUMINIUM AND HOT PRESSED AT 1400°C, 20 MPA AND 1 HOUR	139
TABLE 6.3.6: DENSITY, RELATIVE DENSITY AND POROSITY FOR ALMGB <sub>14</sub> PREPARED AT 900°C, 1200°C, 1400°C, 1500°C, 1600°C AND 1700°C	143
TABLE 6.3.7: THE DENSITY, POROSITY AND ALMGB <sub>14</sub> :MGAL <sub>2</sub> O <sub>4</sub> MAJOR PEAK RATIO FOR SAMPLES PREPARED AT 20 MPA AND 75 MPA AT 1600°C	144
TABLE 6.3.8: A COMPARISON OF THE DENSITIES OBTAINED FROM PRE-REACTED POWDERS AND ELEMENTAL POWDERS AT 1400°C AND 20 MPA	145
TABLE 6.3.8: DENSITIES, POROSITIES FOR ELEMENTAL AND PRE-REACTED POWDERS PREPARED AT 1600°C AND 75 MPA	146
TABLE 6.3.9: THE KNOOP HARDNESS OF COMPOSITES PREPARED IN TABLE 6.3.8 AT A 500 G LOAD	149
TABLE 6.3.10: A SUMMARY OF THE CRYSTALLINE PHASES IDENTIFIED BY XRD IN THE COMPOSITES	174
TABLE 6.3.10: DENSITY, POROSITY, VICKERS HARDNESS AND FRACTURE TOUGHNESS FOR THE COMPOSITES	176
TABLE 6.3.11: COMPARISON OF THE CHANGE IN HARDNESS	177
TABLE 1: COMPOSITIONS FOR THE PHASE DIAGRAM	191
TABLE 2: MASS AND ATOMIC PERCENTS FOR ALMGB <sub>14</sub>	191
TABLE 3: COMPOSITIONS FOR THE COMPOSITES PREPARED AT 1600°C	192